Supporting Information

Nanocavity-Confined Cu_2O in Porphyrin-based MOF for Steering CO_2 Electroreduction toward Hydrocarbons

Peng Liu[a], Xinqi Pan[a], Shanshan Zheng[a], Li Deng[a], Kejing Shen[a], Shilei Ding[b], Ruoyu Chen[c], Zhifeng Xin[a]*

[a] Institute of Molecular Engineering and Applied Chemistry, Anhui University of Technology, Ma'anshan, Anhui 243002, P. R. China.

[b] School of Energy and Environment, Anhui University of Technology, Ma'anshan 243002, China.

[c] School of Metallurgical Engineering, Anhui University of Technology, Maanshan, Anhui 243002, China1 The two authors are equally contributed.

* Correspondence and requests for materials should be addressed to Z. X. (email: xinzf521@ahut.edu.cn).

Materials: 4-Formylbenzoic acid, N,N-dimethylformamide (DMF), copper(II) sulfate pentahydrate ($CuSO_4 \cdot 5H_2O$), ascorbic acid, zirconyl chloride octahydrate ($ZrOCl_2 \cdot 8H_2O$), dichloroacetic acid, sodium hydroxide (NaOH), pyrrole, absolute ethanol (C_2H_5OH), acetone, and anhydrous methanol (CH_3OH) were purchased from Sinopharm Chemical Reagent Co., Ltd. High-purity gases (CO_2 and N_2, purity ≥ 99.99%) were supplied by Nanjing Special Gas Co., Ltd., and ^{13}C-labeled carbon dioxide ($^{13}CO_2$, isotopic purity 99%) was obtained from Cambridge Isotope Laboratories (USA). Ultrapure water (resistivity 18.25 MΩ·cm) was prepared using a Fulham Ultra-Pure Water System (Qingdao, China). All chemicals and reagents were used as received without further purification.

Product Analysis: Gaseous reduction products were analyzed using a Shimadzu GC-2010 gas chromatograph equipped with a flame ionization detector (FID) and a thermal conductivity detector (TCD), using N_2 as the carrier gas. Liquid-phase products were quantified by 1H nuclear magnetic resonance (NMR) spectroscopy (Bruker Avance II 400 MHz). For analysis, 0.4 mL of the electrolyte was mixed with 0.1 mL deuterated dimethyl sulfoxide (DMSO-d6, 99.99%).

Faradaic Efficiency (FE) Calculation

The Faradaic efficiency was calculated as follows[1]:

$$FE = \frac{(N \times n \times F)}{Q} \times 100\%$$

where:

Q = total charge passed (Coulombs, C), F = Faraday constant (96485 C mol^{-1}),

N = moles of product generated, N = number of electrons required for product formation (e.g., H_2: 2; CO: 2; CH_4: 8; C_2H_4: 12).

Theoretical calculation： All first-principles Density Functional Theory (DFT) calculations were performed to investigate the geometric and electronic structures of key reaction

intermediates (e.g., *CO_2, *COOH, *CO, *CHO, *OCH_3, *OHCCHO) and to evaluate the thermodynamic feasibility of the proposed pathways. The simulations were carried out using the Vienna Ab Initio Simulation Package (VASP) with the generalized gradient approximation (GGA-PBE) exchange-correlation functional[2,3], incorporating Grimme's DFT-D3 dispersion correction to account for van der Waals interactions. The projector-augmented wave (PAW) method was employed to describe core electrons[4], while a plane-wave basis set with a kinetic energy cutoff of 400 eV was adopted for valence electrons. The calculations were performed with a kinetic energy cutoff of 450 eV and the Perdew-Burke-Ernzerhof (PBE) functional [5] for exchange-correlation interactions. Gibbs free energy changes (ΔG) for each elementary step were computed as:

$$\Delta G = \Delta E_{DFT} + \Delta E_{ZPE} - T\Delta S + \Delta G_{solv} + \Delta G_{pH}$$

Where ΔE_{DFT} denotes the DFT total energy difference, ΔE_{ZPE} the zero-point energy correction (derived from vibrational frequency analysis), $T\Delta S$ the entropic contribution, ΔG_{solv} the solvation energy (implicit solvent model), and ΔG_{pH} the pH-dependent term adjusted via the Nernst equation. Transition states were located using the climbing-image nudged elastic band (CI-NEB) method, with convergence criteria of 10^{-4} eV for electronic self-consistency and 0.04 eV $Å^{-1}$ for ionic relaxation. DFT calculations were conducted using the Vienna Ab initio Simulation Package (VASP), employing plane-wave basis sets with the projector augmented-wave (PAW) pseudopotential method.

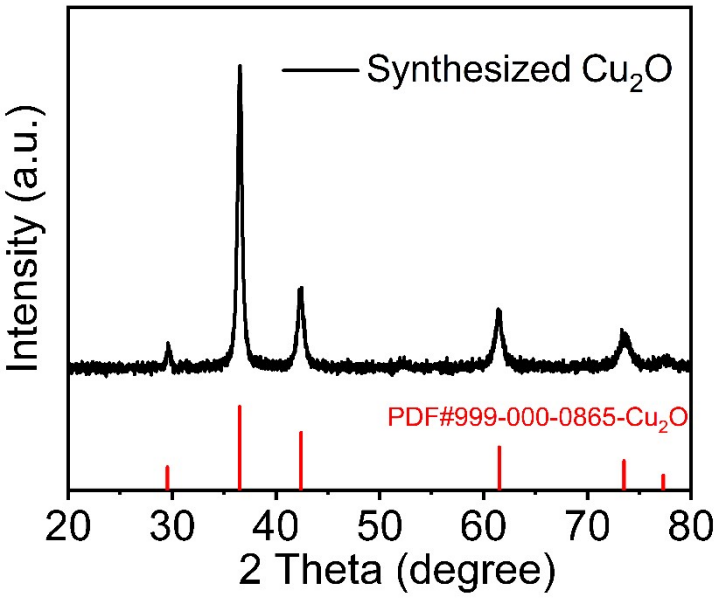

Fig. S1. PXRD pattern of the synthesized Cu_2O nanoparticles.

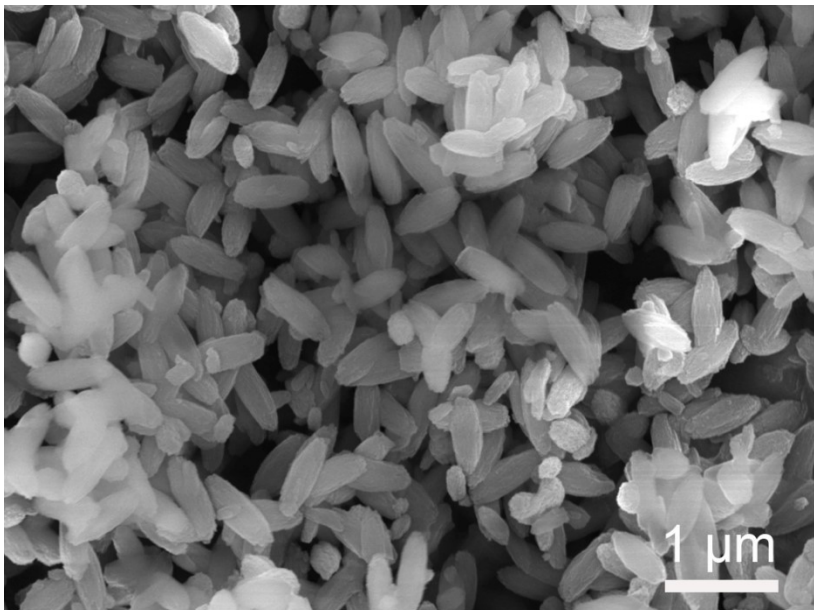

Fig. S2. SEM image of synthesized PCN-223.

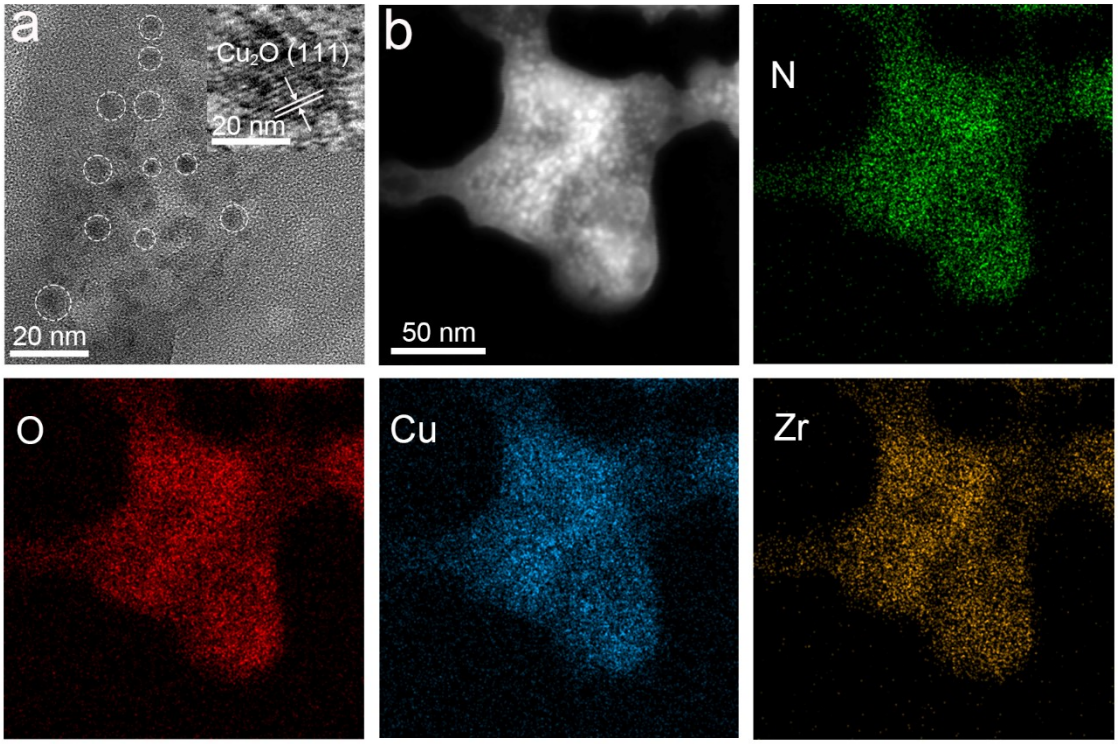

Fig. S3. Morphological characterization of ground Cu_2O@PCN-223. (a) HRTEM image, (b) STEM image and corresponding EDX elemental mapping.

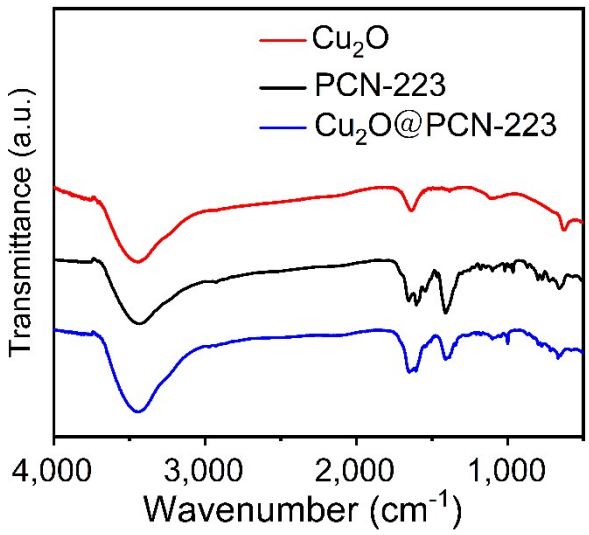

Fig. S4. FT-IR spectra of Cu_2O@PCN-223, PCN-223, and Cu_2O.

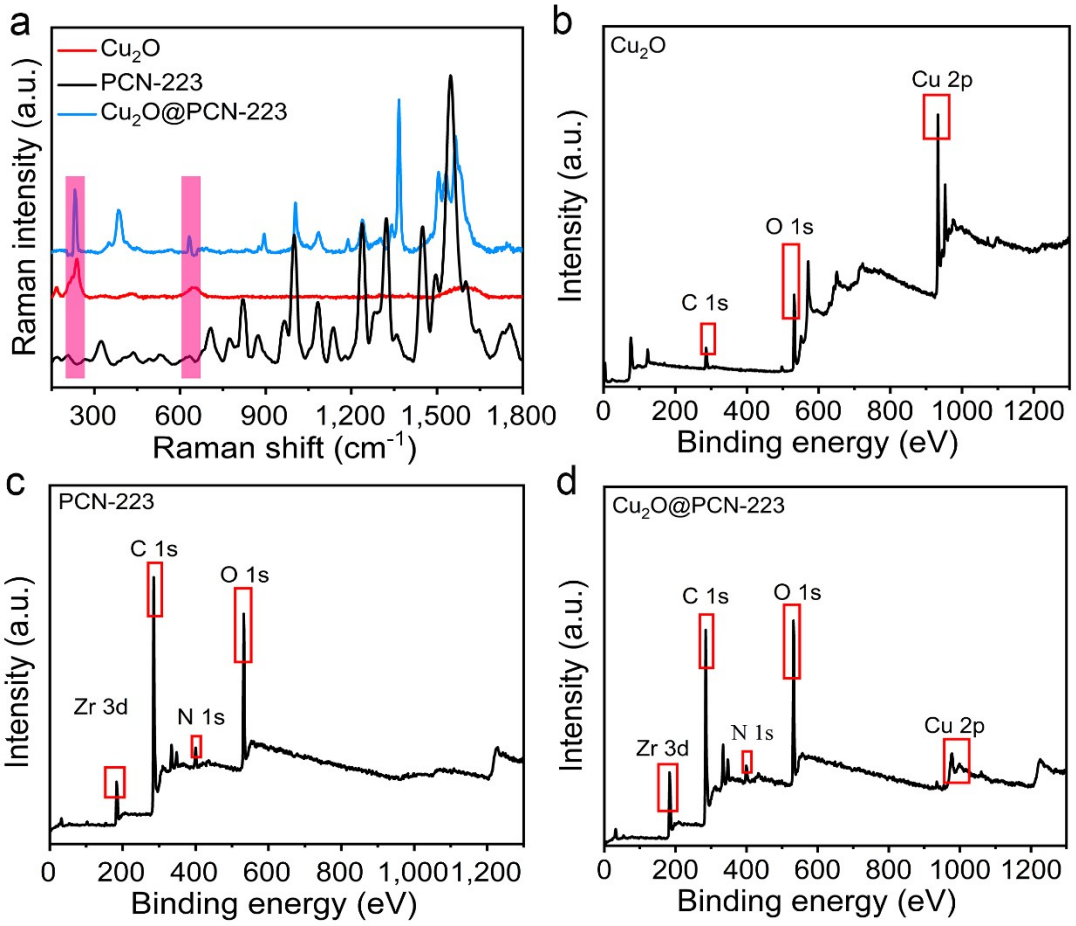

Fig. S5. Characterization of Cu_2O@PCN-223, PCN-223, and Cu_2O. (a) Raman spectra, (b) XPS spectrum of Cu_2O; (c) XPS spectrum of PCN-223; (d) XPS spectrum of Cu_2O@PCN-223.

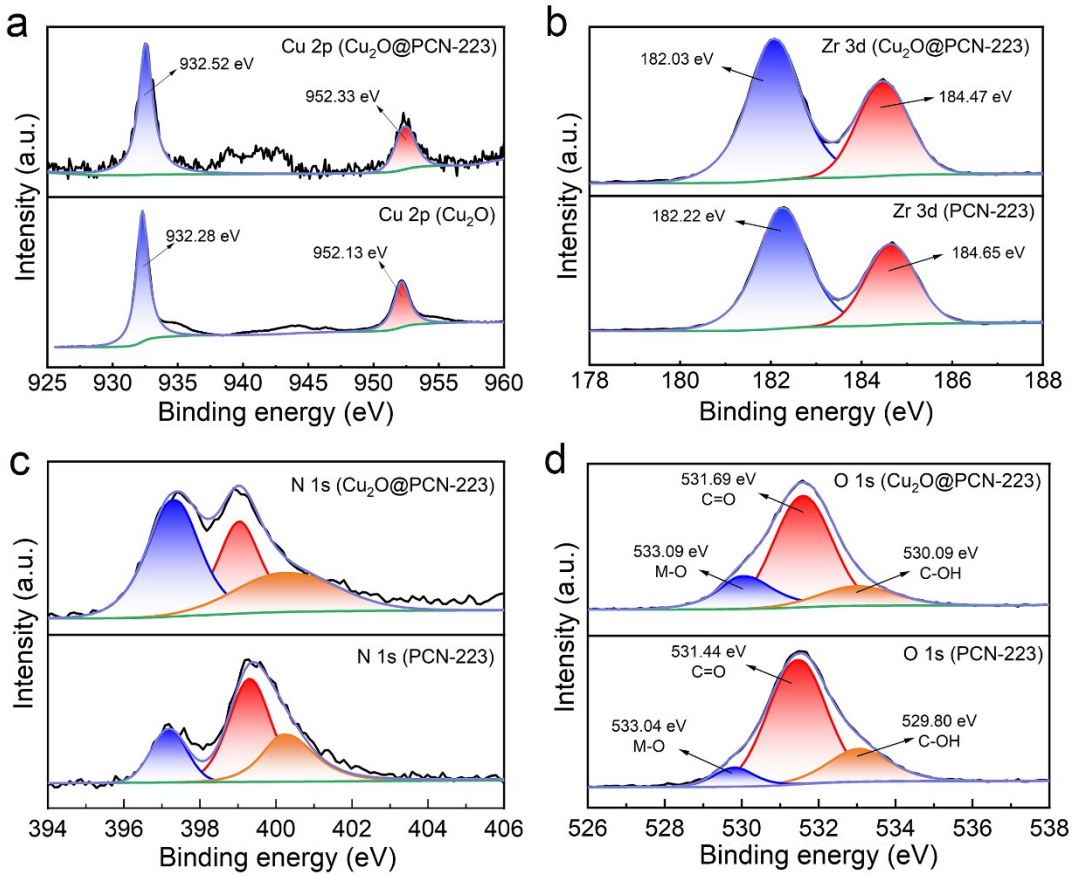

Fig. S6. High-resolution XPS spectra. (a) Cu 2p scan, (b) Zr 3d scan, (c) C 1s scan, (d) N 1s scan, and (e) O 1s scan.

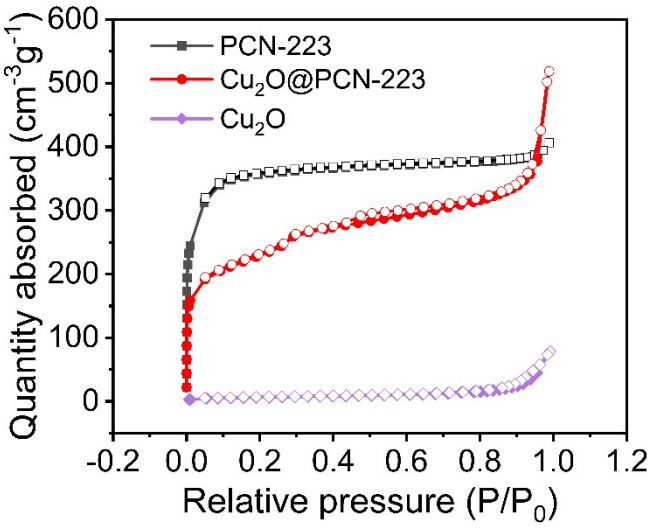

Fig. S7. N_2 adsorption-desorption isotherms of PCN-223, Cu_2O and Cu_2O@PCN-223.

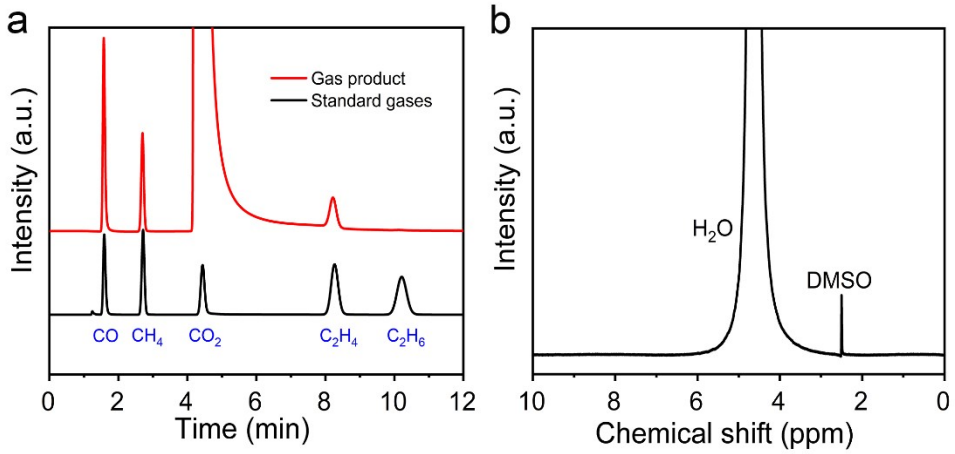

Fig. S8. Characterization of CO_2RR products catalyzed by Cu_2O@PCN-223. (a) Gas chromatogram, (b) ^1H NMR spectrum.

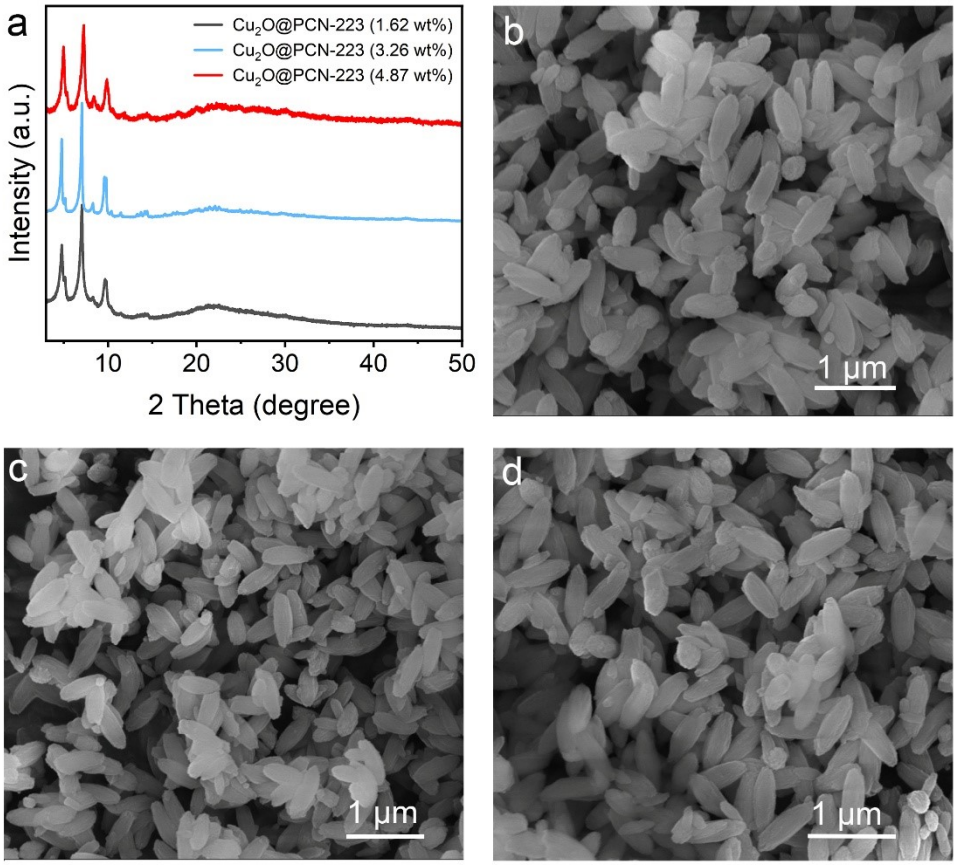

Fig. S9. Characterization of Cu_2O@PCN-223 with different Cu_2O loadings. (a) PXRD patterns. (b) SEM image of Cu_2O@PCN-223 (1.62 wt%). (c) SEM image of Cu_2O@PCN-223 (3.26 wt%). (d) SEM image of Cu_2O@PCN-223 (4.87 wt%).

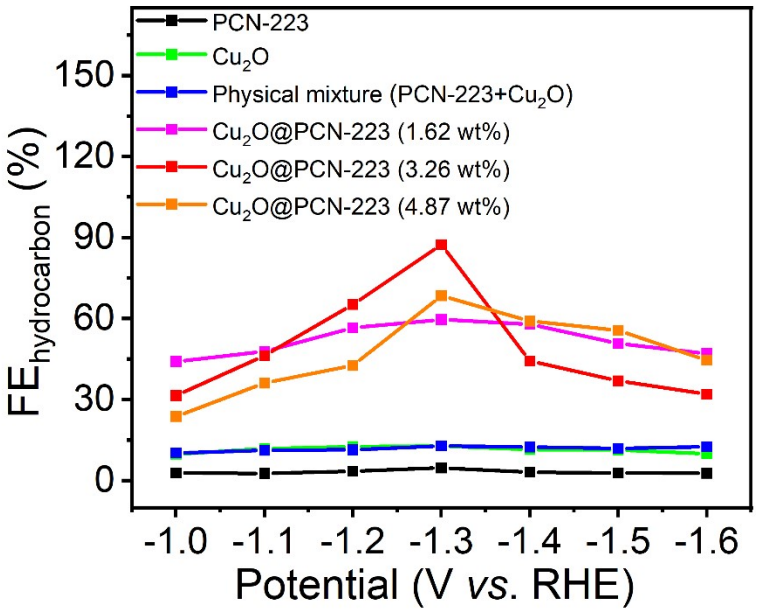

Fig. S10. Comparison of $FF_{hydrocarbons}$ between Cu_2O@PCN-223 and the reference sample.

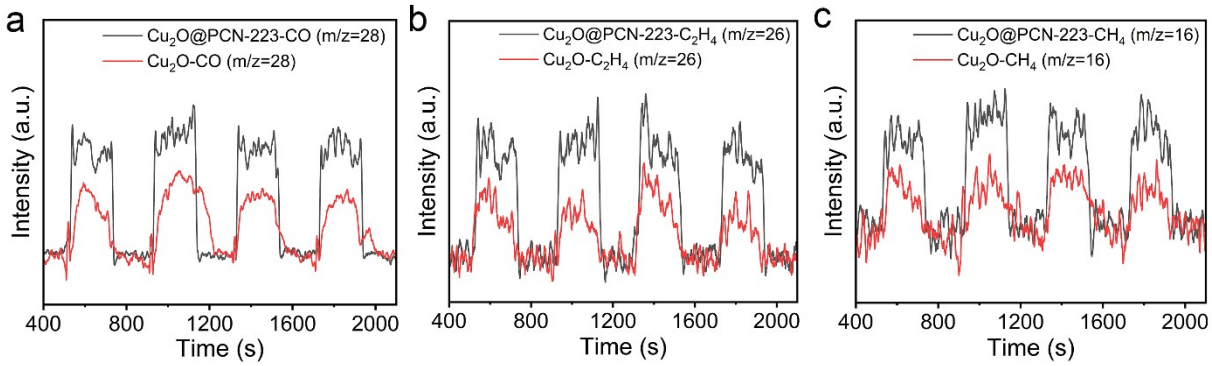

Fig. S11. Online differential electrochemical mass spectrometry (DEMS) of Cu_2O@PCN-223 at a constant potential of −1.3 eV. (a) CO, (b) CH_2=CH_2, (c) CH_4.

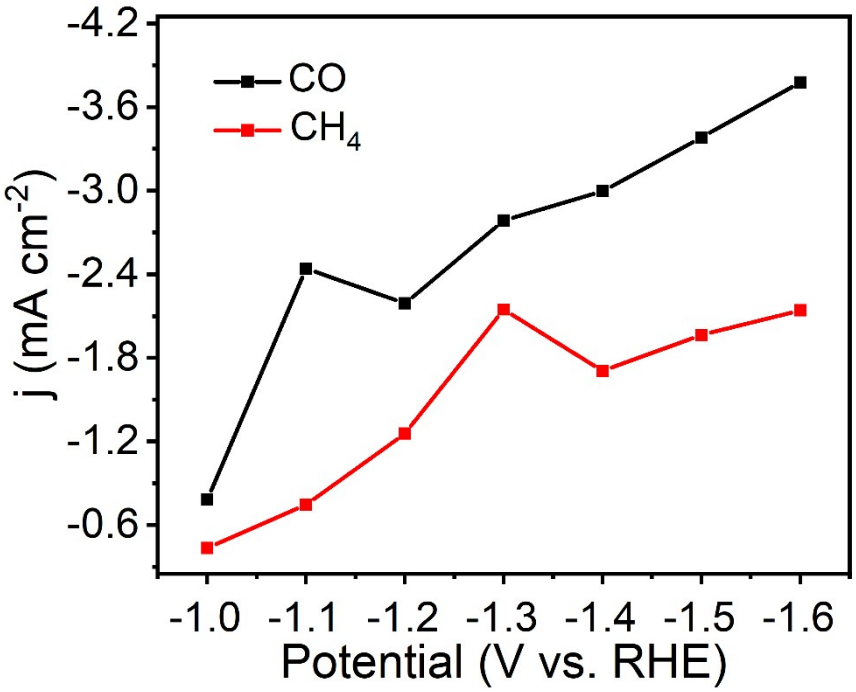

Fig. S12. Partial current densities of gaseous products obtained from PCN-223 at various applied potentials.

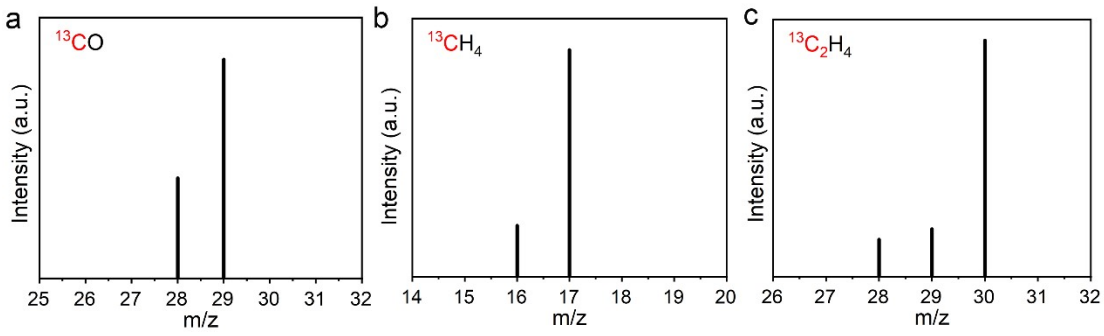

Fig. S13. Mass spectra for gas products. (a) ^{13}CO; (b) $^{13}CH_4$; (c) $^{13}C_2H_4$.

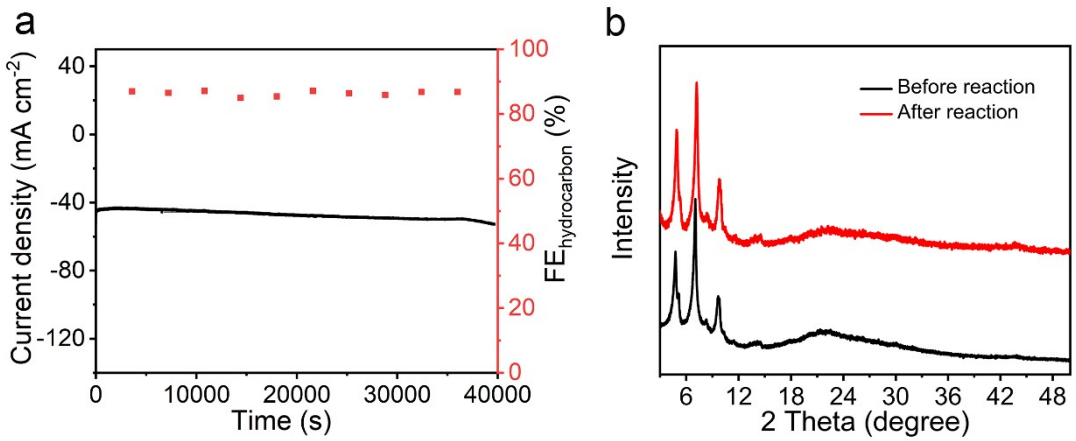

Fig. S14. Stability tests of Cu_2O@PCN-223. (a) Durability test of Cu_2O@PCN-223 at -1.3 V vs. RHE. b) PXRD patterns before and after reaction.

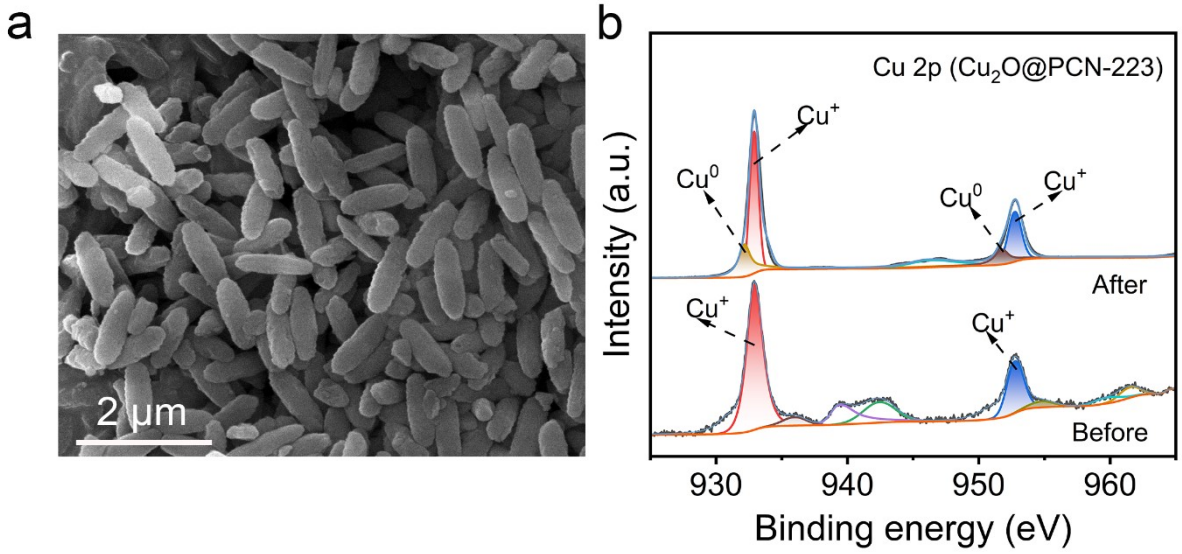

Fig. S15. (a) SEM image of Cu_2O@PCN-223 after the reaction. (a) XPS spectra of Cu_2O@PCN-223 before and after the reaction

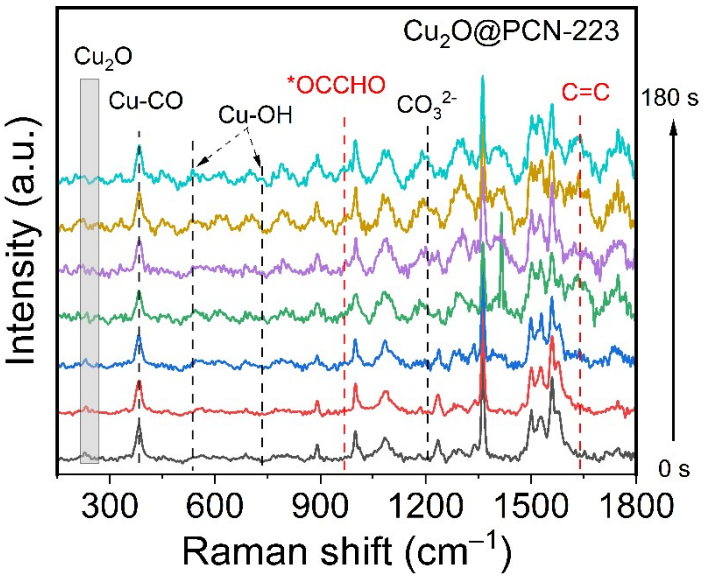

Fig. S16. In-situ Raman spectra of Cu_2O@PCN-223 at different time points

Table S1 BET surface area and pore volume of Cu_2O@PCN-223 and PCN-223 calculated from N_2 adsorption data.

Catalyst	Surface area (m^2/g)	Median pore width (Å)	Pore volume (cm^3/g)
PCN-223	1065.56	5.871	0.546
Cu_2O	22.57	11.247	0.118
Cu_2O@PCN-223	791.04	5.822	0.339

Table S2 Copper (Cu) content in Cu_2O@PCN-223 with different cuprous oxide (Cu_2O) loadings analyzed by inductively coupled plasma (ICP) testing.

Samples	Cu (wt%)	Cu_2O (wt%)
Cu_2O@PCN-223	1.44	1.62
Cu_2O@PCN-223	2.90	3.26
Cu_2O@PCN-223	4.33	4.87

Table S3 Comparison of Cu_2O@PCN-223 with previously reported MOF electrocatalysts for CO_2RR to produce ethylene and methane

Catalyst	FE_{C2H4}	FE_{CH4}	FE_{CH}	Potential	Stability	Ref
Cu_2O@PCN-223	48.7	38.6	87.3	-1.3 v	11 h	This work
Au-NN@PCN-222(Cu)	52.5	5.0	57.5	-1.2 v	10 h	6
CPFs	18.0	56.0	74.0	-1.4 v	2 h	7
Cu@ZIF-8	-	-	57.5	-0.7 v	6.5 h	8
Cu_1Ni-BDP	52.7	-	~52.7	-1.3 v	28 h	9
Lu-HHTP	-	77.0	77.0	-1.1 v	150 h	10
Cu^{II}/ade-MOF	45 (1.4)	50 (1.6)	73.0	-1.6 v	8 h	11
S-HKUST-1	60.0	5.6	65.6	-1.3 v	480 h	12
Sn-THO	-	46.5	46.5	-1.6 v	80 h	13
2Bn-Cu@Uio-67	-	81.0	~81.0	-1.5 v	-	14
NNU-50	15.1	66.4	81.5	-1.0 v	4 h	15
KB@$Cu_3(HITP)_2$	70.0	-	~70.0	-1.4 v	10 h	16
TEMPOL@HKUST-1	44.7	11.5	56.2	-1.8 v	8.3 h	17
Cu_2O@Cu-MOF	16.2	63.2	79.4	-1.7 v	1 h	18
BIC-145	28.0	6.7	34.7	-1.2 v	5 h	19
HATNA-Cu-MOF	-	78.0	~78.0	-1.5 v	12 h	20

References:

1 X.L. Xie, X. Zhang, M. Xie, L.K. Xiong, H. Sun, Y.T. Lu, Q.Q. Mu, M.H. Rummeli, J.B. Xu, S. Li, J. Zhong, Z. Deng, B.G. Ma, T. Cheng, W.A. Goddard, Y. Peng, *Nat Commun*, 2022, **13**, 63.

2 G. Kresse, J. Furthmüller, Phys. Rev. B, 1996, **54**, 11169–11186.

3 G. Kresse, J. Furthmüller, Comput. Mater. Sci, 1996, **6**, 15–50.

4 P.E. Blöchl, Phys. Rev. B, 1994, **50**, 17953–17979.

5 J.P. Perdew, K. Burke, M. Ernzerhof, Phys. Rev. Lett, 1996, **77**, 3865–3868.

6 Xie, X., Zhang, X., Xie, M. et al. Nat Commun, 2022, **13**, 63

7 Y.Z. Zhou, S.H. Chen, S.B. Xi, Z.T. Wang, P.L. Deng, F. Yang, Y.J. Han, Y.J. Pang, B.Y. Xia, Cell Rep Phys Sci, 2020, **1**, 100182.

8 B. Sun, H. Hua, H.C. Liu, J.Y. Guan, K.X. Song, C.R. Shi, H.Y. Cheng, J. Colloid Interface Sci, 2024, **661**, 831 – 839.

9 L. Huang, Z.A. Liu, G. Gao, C.L. Chen, Y.R. Xue, J.W. Zhao, Q. Lei, M.T. Jin, C.Q. Zhu, Y. Han, J.S. Francisco, and X. Lu, J. Am. Chem. Soc, 2023, **145**, 26444-26451.

10 F.Q. Yu, G.Y. Zhang, M.X. Shu, H.M. Wang, Angew. Chem. Int. Ed, 2025, **64**, e202416467.

11 F. Yang, A.L. Chen, P.L. Deng, Y.Z. Zhou, Z. Shahid, H.F. Liu, B.Y. Xia, Chem. Sci, 2019, **10,** 7975.

12 C.F. Wen, M. Zhou, P.F. Liu, Y.W. Liu, X.F. Wu, F.X. Mao, S. Dai, B.B. Xu, X.L. Wang, Z. Jiang, P. Hu, S. Yang, H.F. Wang, H.G. Yang, Angew. Chem. Int. Ed, 2022, **61**, e202111700.

13 Z.H. Zhao, J.R. Huang, P.Q. Liao, X.M. Chen, Angew. Chem. Int. Ed, 2023, **62**, e202301767.

14 S.H. Chen, W.H. Li, W.J. Jiang, J.R. Yang, J.X. Zhu, L.G. Wang, H.H. Ou, Z.C Zhuang, M.Z. Chen, X.H Sun, D.S. Wang, Y.D. Li, Angew. Chem. Int. Ed, 2022, **61**, e202114450.

15 L.Z. Dong, Y.F. Lu, R. Wang, J. Zhou, Y. Zhang, L. Zhang, J. Liu, S.L. Li, Y.Q. Lan, Nano Res, 2022, **15**, 10185–10193.

16 H. Sun, L. Chen, L.K. Xiong, K. Feng, Y.F. Chen, X. Zhang, X.Z. Yuan, B.Y. Yang, Z. Deng, Y. Li, M.H. Rümmeli, J. Zhong, Y. Jiao, Y. Peng, Nat Commun, 2021, **12**, 6823.

17 B.P. Yin, C. Wang, S.J. Xie, J.M. Gu, H. Sheng, D.X. Wang, J.N. Yao, C. Zhang, Angew. Chem. Int. Ed, 2024, **63**, e202405873.

18 X.Y. Tan, C. Yu, C.T. Zhao, H.W. Huang, X.C. Yao, X.T. Han, W. Guo, S. Cui, H.L. Huang, J.H. Qiu, ACS Appl. Mater. Interfaces, 2019, **11**, 9904-9910.

19 J.Q. Chen, Q.H. Li, Q.L. Hong, P. Shao, H.X. Zhang, J. Zhang, Sci. China Chem, 2025, **68,** 943–950.

20 Y.Z. Liu, S. Li, L. Dai, J.N. Li, J.N. Lv, Z.J.J. Zhu, A.X. Yin, P.F. Li, B. Wang, Angew. Chem. Int. Ed, 2021, **60**, 16409 – 16415.